

## Control of Polymer Crystallization by Pseudo-Polyrotaxane Nanosheets

Cong Liu, Sinan Feng, Shuntaro Uenuma,\* Shota Ando, Hideaki Yokoyama, Atsushi Takahara, and Kohzo Ito\*



Cite This: *Macromolecules* 2025, 58, 451–458



Read Online

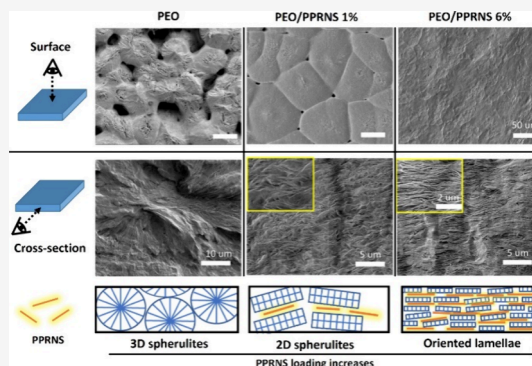
ACCESS |

Metrics & More

Article Recommendations

Supporting Information

**ABSTRACT:** We present a straightforward yet highly efficient approach for controlling the orientations of poly(ethylene oxide) (PEO) lamellae by introducing pseudopolyrotaxane nanosheets (PPRNSs), a novel class of two-dimensional fillers featuring well-organized polymer brushes. Grazing-incidence wide-angle X-ray scattering reveals parallel alignments of uniformly flat-on PEO lamellae to the film surface, and the degrees of their orientations are closely linked to the PPRNS concentration. Via control experiments and comprehensive investigations of crystallization kinetics and morphological evolutions of nanocomposites with different PPRNS contents, we elucidate the mechanism driving lamellar orientation. PPRNSs provide additional nucleation sites for PEO crystallization, thereby influencing the crystallization kinetics. PPRNSs, acting as nucleating agents, accelerate crystallization rates, impacting crystal morphology, crystal growth direction, and crystallinity preservation. Control experiments emphasize the distinct roles of polymer brushes in offering nucleation sites. This study lays the foundation for diverse applications and further explorations of PPRNS-based materials in the fields of polymer nanocomposites, surface engineering, and functional material design.



### INTRODUCTION

Crystal orientation is an important factor affecting the properties, such as strength,<sup>1</sup> modulus,<sup>2</sup> optical anisotropy,<sup>3</sup> gas permeability,<sup>4</sup> thermal conductivity,<sup>5</sup> etc., of semicrystalline polymers.<sup>6,7</sup> Extensive approaches, including epitaxial crystallization,<sup>8</sup> stress-induced crystallization,<sup>9</sup> multiple layer coextrusion,<sup>10</sup> nanofiller-induced crystallization,<sup>11</sup> and related techniques,<sup>12,13</sup> have been used to control the degree of crystal orientation and structures of crystallites. Among all strategies, introduction of two-dimensional (2D) nanofillers into semicrystalline polymers represents a simple way to regulate the crystalline structures of semicrystalline polymers due to the high surface areas and strong confinement effects of these nanofillers. For example, graphene<sup>14</sup> and nanoclays<sup>15</sup> confine semicrystalline polymers into a quasi-2D crystal growth. Theoretically, this strategy offers multiple advantages, namely reduced processing limitations, tunable orientation degree, and enhanced mechanical properties of the resulting polymers. However, to achieve successful control of crystalline orientation, several requirements, including excellent dispersion states and high volume fractions of nanofillers and outstanding compatibility between nanofillers and polymer matrix, need to be met.<sup>16</sup> Additionally, acknowledging that although confinement effects enable achievable crystalline orientation, they often cause the loss of overall crystallinity is essential.<sup>17,18</sup> Consequently, the exploration of advanced

materials or strategies for fine-tuning polymer crystallization is urgently required.

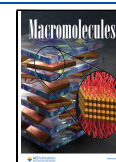
Pseudopolyrotaxane nanosheets (PPRNSs) are a novel type of 2D nanofillers comprising cyclodextrin (CD) and biocompatible poly(ethylene oxide)-*block*-poly(propylene oxide)-*block*-poly(ethylene oxide) (PEO-*b*-PPO-*b*-PEO) triblock copolymers.<sup>19–21</sup> CD rings selectively cover the central PPO segment, resulting in an inclusion complex that assembles into 2D nanosheets (Figure 1). Organic compositions of PPRNSs render them nontoxic and biocompatible. Thickness of the CD layer is determined by the extended length of the PPO segment, which adopts an all-*trans* conformation and measures 11 nm in length.<sup>20</sup> Notably, unlike other 2D nanofillers, PPRNSs possess well-organized polymer brushes grafted onto their surfaces.<sup>19</sup> Polymer brushes exhibit capacities to enhance nanoparticle dispersion, utilizing the synergy between entropy-driven processes and enthalpic interactions.<sup>22,23</sup> Contrary to conventional methods of polymer brush synthesis, which often encounter challenges such as

**Received:** September 4, 2024

**Revised:** November 19, 2024

**Accepted:** December 16, 2024

**Published:** December 26, 2024



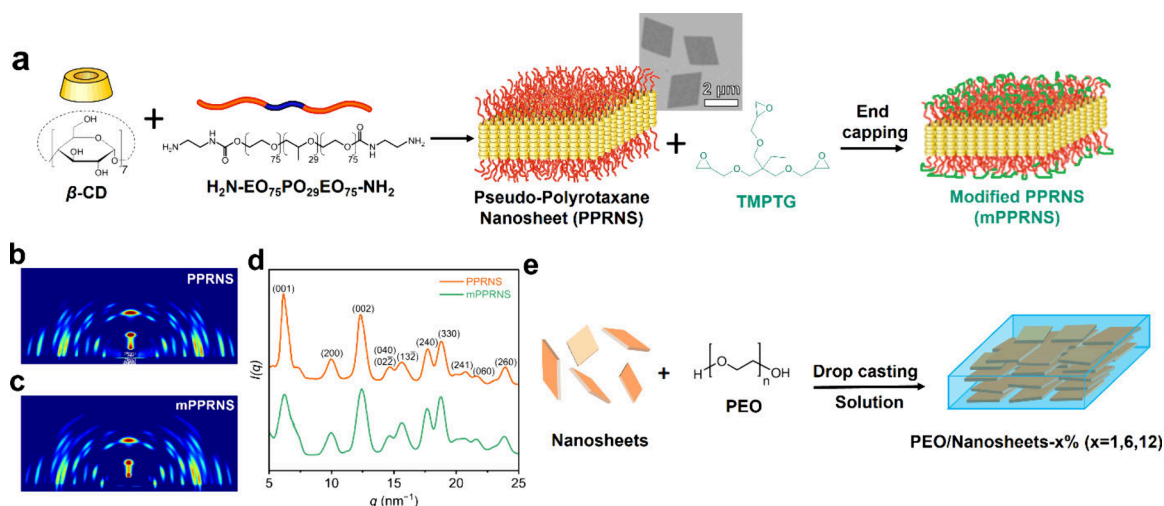


**Figure 1.** (a) Syntheses of pseudopolyrotaxane nanosheets (PPRNSs) and end-capped PPRNSs (mPPRNSs) along with scanning electron microscopy (SEM) and atomic force microscopy (AFM) images with scale bars of 2 and 1  $\mu\text{m}$ , respectively. (b and c) Grazing-incidence wide-angle X-ray scattering (GI-WAXS) patterns. (d) One-dimensional profiles with assigned crystal planes. (e) Schematics of the fabrications of poly(ethylene oxide) (PEO)/nanosheet (PPRNS or mPPRNS) nanocomposite films.

laborious preparations and difficulty in regulating grafting length and density, the utilization of self-assembly enables facile and large-scale production of PPRNSs. Furthermore, precisely defined structures of PPRNSs facilitate accurate control over the grafting densities and lengths of polymer brushes, offering promising solutions to current challenges in nanoparticle dispersion. Although previous studies have suggested the roles of polymer brushes in providing nucleation sites, thus potentially enhancing crystallization,<sup>24,25</sup> this phenomenon has not been clearly established for 2D materials. Consequently, our objective is to investigate the capacities of PPRNSs to influence crystallization behaviors, particularly crystal orientation, of semicrystalline polymers.

Herein, we introduce a novel strategy utilizing the unique characteristics of PPRNSs to achieve precise regulation of the crystallization structures of semicrystalline polymers. This approach combines the confinement effects typical of conventional methods with epitaxial crystallization induced by the well-organized grafted polymer brushes. PEO was chosen as the polymer matrix owing to its chemical compatibility with the polymer brushes on PPRNSs, ensuring efficient dispersions and compatibilities of PPRNSs. Previous research indicates that PEO brushes on PPRNSs preferentially form flat-on crystals.<sup>26</sup> We anticipate that the growths of PEO crystals can be directed using the above-mentioned characteristic along with the organized polymer brushes, thereby enhancing control over crystalline orientation.

To highlight the significance of polymer brushes, control experiments are conducted to disrupt the polymer brushes by capping their ends with triple epoxide groups.<sup>27</sup> This leads to a structure lacking free extended polymer brushes, similar to those of conventional 2D materials. Detailed characterization of crystallization orientation via X-ray studies and examination of crystallization kinetics are performed to elucidate the crystallization mechanism. Distinct features of PPRNSs as novel 2D fillers are also discussed. We believe that new biorelated materials with considerably high performances can be developed by manipulating crystal orientation and modifying the physical properties of PEO nanocomposites films (NCFs) using PPRNSs. Because of their unique

properties, PPRNSs are promising candidates for advancing high-performance polymer nanocomposites, specifically in the fields of biotechnology and energy storage electronics.

## MATERIALS AND METHODS

**Materials.** Beta-cyclodextrin ( $\beta$ -CD) and tetrahydrofuran were purchased from Fujifilm Wako Pure Chemical Corporation. HO-PEO<sub>75</sub>-*b*-PPO<sub>30</sub>-*b*-PEO<sub>75</sub>-OH (Pluronic F68), carbonyldiimidazole (CDI), ethylenediamine and trimethylolpropane triglycidyl ether (TMPTG) were procured from Sigma-Aldrich. PEO with a weight-average molecular weight of 330 000 g/mol and polydispersity of 1.18 was purchased from Polymer Source. All chemicals were used as received.

**Synthesis of H<sub>2</sub>N-PEO<sub>75</sub>-*b*-PPO<sub>30</sub>-*b*-PEO<sub>75</sub>-NH<sub>2</sub>.** Pluronic F68 (10.0 g, 1.2 mmol) was dissolved in tetrahydrofuran (80 mL) to prepare solution A. Then, CDI (1.96 g, 12 mmol) was dissolved in tetrahydrofuran (10 mL) to prepare solution B. Solution A was dropwise added to solution B, which turned milky, at room temperature. After the mixed solution was stirred for 4 h, ethylenediamine (7.9 mL) was introduced into the resulting solution. Reaction was performed at room temperature for 17 h. Entire reaction was conducted under the protection of N<sub>2</sub> gas. The reaction was terminated by adding water (2.5 mL) to the reaction mixture. Product was concentrated by rotary evaporator and purified by dialysis in water. Finally, after drying the product using a freeze-dryer for 24 h, a white powder was obtained.

**Preparation of Water-Dispersed Samples of PPRNSs and mPPRNSs.** Nanosheets were fabricated using a previously reported procedure.<sup>20</sup> H<sub>2</sub>N-PEO<sub>75</sub>-*b*-PPO<sub>30</sub>-*b*-PEO<sub>75</sub>-NH<sub>2</sub> (1.08 g) was added to a  $\beta$ -CD aqueous solution (100 mL, 18 g/L). The mixed solution was stirred for 2 weeks at room temperature and gradually became turbid during PPRNS formation. Surface-modified PPRNSs were synthesized following a revised procedure.<sup>27</sup> TMPTG (100 equiv vs NH<sub>2</sub>) was introduced into an aqueous PPRNS dispersion and allowed to undergo ring-opening reaction with terminal NH<sub>2</sub> groups at room temperature for 1 week.

**Fabrication of PEO and PEO/PPRNS NCFs.** PEO and  $\beta$ -CD mixed solution was prepared by dissolving PEO (50 mg/mL) and  $\beta$ -CD (18 mg/mL) in water. PPRNSs were acquired by centrifugation and then mixed with the PEO and  $\beta$ -CD solution in a predetermined weight ratio followed by mechanical stirring for 1 h. The blend solution was cast in a polytetrafluoroethylene Petri dish ( $\varnothing$  15 cm) or on a Si wafer (25  $\times$  25 cm<sup>2</sup>). Films were achieved after drying in room

temperature for 1 week. This procedure resulted in a 100–200- $\mu\text{m}$ -thick composite film.

**Characterization.** Scanning electron microscopy (SEM) images were obtained using a JEOL JSM-7800F field-emission scanning electron microscope. Grazing incidence wide-angle X-ray scattering (GI-WAXS) experiments were conducted using Rigaku SmartLab with a HyPix-3000 detector. X-ray wavelength of 0.154 nm was employed, and the sample-to-detector distance was 67.15 mm. Measurements were performed at an incident angle of  $0.2^\circ$ , which is slightly above the critical angle of the samples. GI-WAXS data processing, including the conversion of 2D diffraction patterns to 1D intensity profiles as a function of the scattering vector  $q$ , where  $q = (4\pi \sin \theta)/\lambda$ , was performed using Rigaku 2DP software. Differential scanning calorimetry (DSC) was performed using Thermo plus EVO2 DSCvesta (Rigaku, Tokyo, Japan) at a heating/cooling rate  $10^\circ\text{C}/\text{min}$ . For isothermal crystallization, specimens were melted at  $100^\circ\text{C}$ . Specimens were maintained at  $100^\circ\text{C}$  for 5 min followed by rapid cooling at  $50^\circ\text{C}/\text{min}$  to crystallization temperature ( $T_c$ ). A new specimen was used for each isothermal test. The crystallinity ( $X_c$ ) was calculated from  $X_c = \Delta H/\Delta H_m^0$  where  $\Delta H$  is the measured melting enthalpies,  $\Delta H_m^0$  is the extrapolated value of the enthalpy corresponding to the melting of a perfect infinite crystalline sample, which was taken as  $197\text{ J/g}$ .<sup>28</sup>

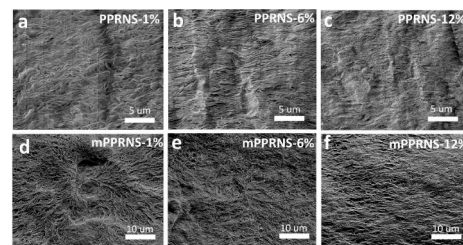
## RESULTS

Figure 1a shows the schematic of the synthesis of PPRNSs. This process involves covering the PPO domain of PEO<sub>75</sub>-*b*-PPO<sub>29</sub>-*b*-PEO<sub>75</sub> with beta ( $\beta$ )-CD rings, forming columns due to higher inclusion force between  $\beta$ -CD and PPO. Subsequent hydrogen bonding drives the assembly of these columns, leading to the formation of 2D nanosheets. Analysis of scanning electron microscopy (SEM) images reveals that the nanosheets demonstrate rhombus shapes with side lengths of approximately one micrometer. End-capped PPRNSs were also prepared using surface-modified variants, referred to as mPPRNSs, based on previous literature.<sup>27</sup> The terminal  $\text{NH}_2$  groups of polymer brushes on PPRNS undergo a ring-opening reaction with epoxide groups in TMPTG, leading to end-capped polymer brushes to form mPPRNSs. This surface modification eliminates the free polymer brush ends, allowing us to study the effect of polymer brush on crystallization. Atomic force microscopy (AFM) image (Supporting Information Figure S1) indicates that the morphologies of mPPRNSs are similar to those of PPRNSs. Grazing-incidence wide-angle X-ray scattering (GI-WAXS) was conducted to label the characteristic peaks of CD and compare the GIWAXS patterns of the two kinds of nanosheets (Figure 1b–d). GI-WAXS patterns of mPPRNSs are identical to those of pristine PPRNSs. Integrated one-dimensional (1D) profiles also suggest that all the reflections (based on a monoclinic unit cell with  $a = 1.910\text{ nm}$ ,  $b = 2.426\text{ nm}$ ,  $c = 1.568\text{ nm}$ , and  $\beta = 111^\circ$ ) are retained after end-capping modification by epoxide.<sup>26</sup> Hence, the structures of PPRNSs remain intact during modification.<sup>27</sup> Delicate modification allows us to elucidate how the polymer brushes on the nanosheet surfaces affect PEO crystallization.

Figure 1e depicts the schematic of the preparation of PEO/PPRNS NCFs. Their synthesis involves mixing PPRNSs and PEO in water, followed by the fabrication of NCFs via drop casting. PPRNS content in NCFs ranges from 1 to 12 wt %. Thicknesses of the resulting NCFs range from 150 to 200  $\mu\text{m}$ . Control experiments were performed using mPPRNSs at equivalent concentrations. Corresponding specimens are labeled as PEO, PEO/PPRNS- $x\%$ , and PEO/mPPRNS- $x\%$ ;  $x\%$  in PEO/PPRNS- $x\%$  and PEO/mPPRNS- $x\%$  represents the

weight percentages of PPRNS and mPPRNS, respectively. Free CD was added to all samples to stabilize PPRNSs and ensure experimental consistency.

To analyze crystal morphology, we employed SEM to observe the surface and cross-section of both PEO films and NCFs containing PPRNSs and mPPRNSs (Figure 2). PEO



**Figure 2.** Cross-sectional SEM images of PEO/PPRNS (a–c) and PEO/mPPRNS (d–f) NCFs.

films (Supporting Information Figures S2 and S3) exhibited large spherulites with an average diameter of  $100\text{ }\mu\text{m}$ , indicating three-dimensional (3D) growth of crystallites. When 1 wt % PPRNSs are introduced into PEO, PEO spherulites tend to generate random polygons from the film surface, implying that the addition of PPRNSs in small amounts alters the crystal growth manner of PEO from 3D to 2D style. In the cross-sectional SEM images shown in Figure 2a–f, the fiber-like structures may represent PEO lamellae. Notably, spherulites are detected in the SEM image of PEO (Supporting Information Figure S3), whereas lamellae are well-aligned parallel to the film surface and stacked along the thickness direction in the SEM images of PEO/PPRNS NCFs. This alignment and condensation of PEO lamellae become more significant with an increase in the PPRNS concentration. Nevertheless, orientations in PEO/mPPRNS NCFs are only observed at a concentration as high as 12 wt %. This difference highlights the crucial role of free polymer brush ends in controlling PEO crystallization behavior.

To explore PPRNS distribution and its impact on PEO chain packing, X-ray analysis was performed. GI-WAXS was used to assess the crystal orientations of PEO lamellae in the presence of PPRNS and mPPRNS in various amounts (Figure 3a–g). 1D profiles integrated along in-plane ( $q_{xy}$ ) and out-of-plane ( $q_z$ ) directions are shown in Figure 3h–k. For PEO, no preferred orientations of crystals are noticed as it demonstrates identical profiles in both directions (dashed line). Reflection peaks at  $q = 13.71$  and  $16.53\text{ nm}^{-1}$  are mainly ascribed to (120) and (032) planes, respectively, based on a monoclinic unit cell with  $a = 8.05\text{ }\text{\AA}$ ,  $b = 13.04\text{ }\text{\AA}$ ,  $c = 19.48\text{ }\text{\AA}$ , and  $\beta = 125.4^\circ$ , where  $c$  is the chain axis.<sup>29</sup> For PEO/PPRNS, the Debye ring exhibited an arc shape, which appeared only in certain ranges of azimuth angle. Moreover, the 1D profiles along  $q_{xy}$  and  $q_z$  directions are quite different. In the  $q_z$  direction (Figure 3i), the intense reflection peaks at  $q = 4.37$  and  $8.74\text{ nm}^{-1}$  are attributed to the (001) and (002) reflections of CD crystals in PPRNSs, respectively. This is in agreement with our previous results<sup>20</sup> and suggests that CD crystals are vertically stacked in head-to-head patterns similar to the cases of pristine PPRNSs. Reflections derived from the (120) and (032) planes of PEO crystals become more anisotropic when the PPRNS loading is higher than 1 wt % due to the evolution of preferred orientations of these crystals. Azimuthal integration profile reveals that the (032) and (120)



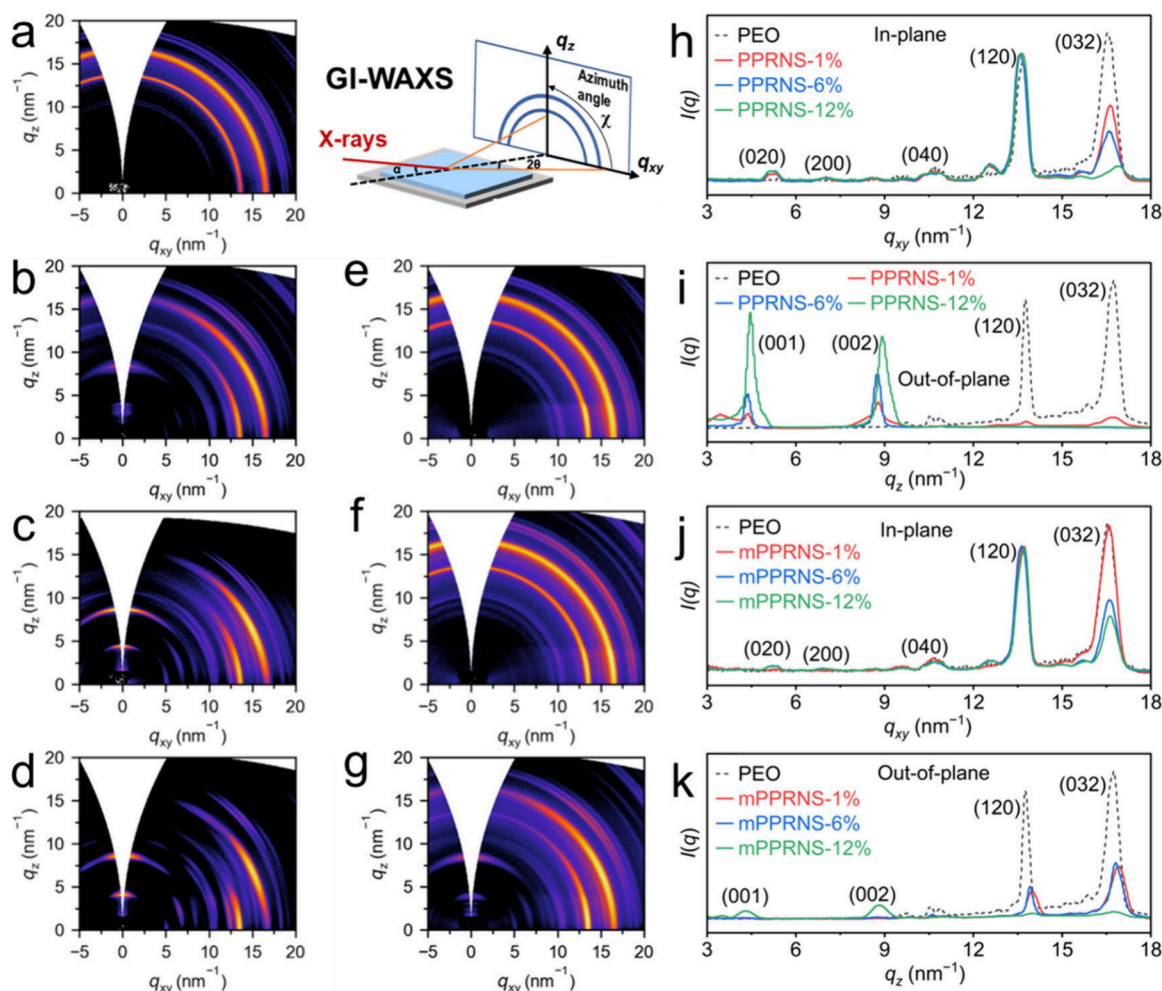


**Figure 3.** GI-WAXS patterns of (a) PEO, (b–d) PEO/PPRNSs, and (e–g) PEO/mPPRNSs. In-plane (h) and out-of-plane (i) profiles of PEO/PPRNSs and in-plane (j) and out-of-plane (k) profiles of PEO/mPPRNSs.

reflections reach their maxima at  $\varphi = 23^\circ$  and  $0^\circ$ , respectively. This indicates that the PEO (032) plane is inclined at  $67^\circ$  with respect to the substrate, whereas the (120) plane is perpendicular to the substrate. Hence, the lamellar PEO crystals are oriented parallel to the film surface, implying the occurrence of flat-on crystallizations of PEO chains in PEO/PPRNS NCFs.

To quantitatively evaluate the impacts of PPRNSs on the degrees of crystalline orientation in PEO lamellae, we analyzed the azimuthal profile of PEO (032) reflection for each sample (Supporting Information Figure S4a). Degrees of crystalline orientation of PEO crystals were determined by the full width at half-maximum (fwhm) (Supporting Information Table S1). Results clearly demonstrate that with an increase in the PPRNS concentration from 1 to 12 wt %, fwhm of PEO (032) decreases from  $31.1$  to  $15.4^\circ$ , indicating a higher degree of crystalline orientation. Additionally, we examined the azimuthal profile of CD (002) reflection for each sample (Supporting Information Figure S4b). PEO/mPPRNS-12% exhibits a significantly broader (002) peak than that in the case of PEO/PPRNS-12% and a fwhm ( $24.5^\circ$ ) comparable to that of PEO/PPRNS-1% ( $23.3^\circ$ ). This result reveals that the alignments of mPPRNSs in the PEO matrix are less ordered than those of PPRNSs. With an increase in the PPRNS loading, PEO/PPRNSs demonstrate smaller fwhm values, which indicates enhanced alignments of PPRNSs. The

observed trend can be ascribed to the high probability of contact between PPRNSs with an increase in the PPRNS concentration, leading to low mobility and entropy of PPRNS. To prevent the decreases in mobility and entropy, the system may exhibit a preference for orientation to maximize packing efficiency.<sup>30,31</sup> Considering the confinement of PEO crystals between PPRNSs, the alignments of PPRNSs become crucial for the degree of PEO crystal orientation. Specifically, the alignments of PPRNSs along the film surfaces strongly suppress the growths of PEO crystals in the out-of-plane direction owing to the existence of 2D nanosheets, which is consistent with the SEM observation.

Onset of crystalline orientation in PEO with the addition of just 1 wt % PPRNSs was an interesting finding, a phenomenon rarely noticed with conventional 2D fillers that typically require higher loadings to stimulate crystalline orientation. However, mPPRNSs, engineered to mimic common 2D fillers, failed to induce effective orientations of PEO crystals at lower loadings ( $\sim 1$  wt %). Notably, no evident preference in PEO crystalline orientation was detected until the mPPRNS concentration reached 12 wt %. This suggests that mPPRNSs predominantly influence the orientations of PEO crystals via a confinement effect, similar to the cases of other traditional 2D materials.<sup>32–35</sup> This result implies that the ends of the tethered chain on PPRNS play important roles in determining the orientations of PEO crystals. Combination of all the above-

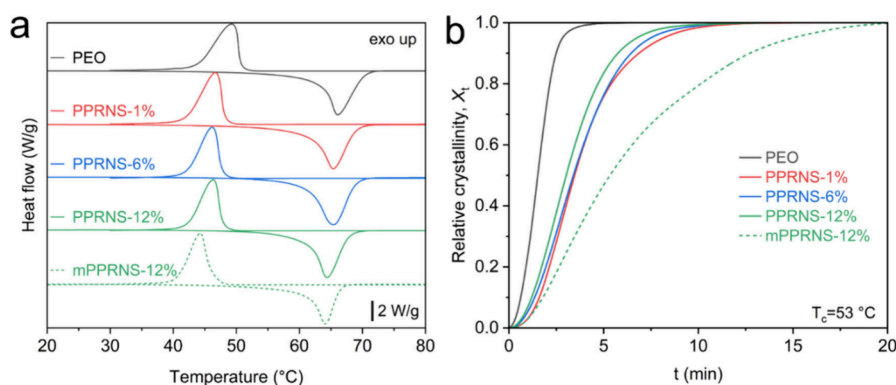


**Figure 4.** Differential scanning calorimetry curves of PEO and PEO/PPRNS NCFs during (a) second heating and first cooling. (b) Relative crystallinity ( $X_t$ ) vs time for isothermal crystallization at the crystallization temperature  $T_c = 53$  °C.

mentioned morphological and crystallographic characterizations indicates that PPRNS demonstrates superior orientation control capability as compared to those of conventional 2D materials.

To understand the crystallization mechanism, we investigated crystallization kinetics using nonisothermal differential scanning calorimetry (DSC) curves (Figure 4a and Table 1).

**Table 1.** Crystallinity ( $X_c$ ), Melting Temperature ( $T_m$ ), Crystallization Temperature ( $T_c$ ), and Crystallization Half-Time ( $t_{1/2}$ ) Values of PEO, PEO/PPRNS NCFs, and PEO/mPPRNS NCFs

	$X_c$	$T_m$ (°C)	$T_c$ (°C)	$t_{1/2}$ (min)
PEO	0.78	66.2	48.9	1.52
PEO/PPRNS-1%	0.82	65.4	46.7	3.47
PEO/PPRNS-6%	0.86	65.3	46.1	3.41
PEO/PPRNS-12%	0.77	64.3	46.4	3.03
PEO/mPPRNS-12%	0.59	63.8	43.8	5.35

Melting temperature ( $T_m$ ), crystallization temperature ( $T_c$ ), and crystallinity ( $X_c$ ) of pristine PEO are 66.2 °C, 48.9 °C, and 0.78, respectively. PEO/PPRNS NCFs exhibit slightly lower  $T_m$  (65.4 °C) and  $T_c$  (46.7 °C) than those of pristine PEO because of the confinement effect.<sup>36</sup> Nevertheless, note that  $T_m$ ,  $T_c$ , and  $X_c$  of PEO/PPRNS NCFs demonstrate negligible variations with changes in the PPRNS content even up to 12 wt %, deviating from expectations exclusively based on confinement effects. In contrast, for PEO/mPPRNS-12%, where confinement dominates,  $T_m$  and  $T_c$  and particularly  $X_c$  are low. This phenomenon is commonly observed in polymer nanocomposites containing 2D fillers,<sup>37–39</sup> in which significant confinement effects inhibit crystallization and interfere with the integrities of polymer crystals, resulting in low  $X_c$  and  $T_c$ .

To gain comprehensive insights into the kinetic aspects of PEO crystallization, we also conducted isothermal DSC at  $T_c = 53$  °C. As shown in Figure 4b, relative crystallinity ( $X_t$ ), defined as the ratio of  $X_c$  at time  $t$  to  $X_c$  when time approaches infinity, was plotted as a function of time, exhibiting a sigmoidal shape characteristic of isothermal polymer crystallization. Introduction of PPRNS, even at a low loading of 1 wt %, increased the crystallization time of PEO, implying significant suppression of crystallization. Inhibition of crystallization in PEO/PPRNS systems can be ascribed to low chain mobility due to the confinement effect.<sup>40</sup> However, with an increase in the PPRNS loading, the crystallization rate gradually and slightly increases (reduced crystallization half-

time  $t_{1/2}$ ), which is an intriguing observation. In addition to the confinement effect, the nucleation effect might contribute to the high crystallization rate. Presence of a nucleating agent enhances the nucleation rate, leading to a higher number of active nuclei and faster crystal growth. When the confinement effect exists to some degree, nucleation strongly influences the crystallization rate.<sup>41</sup> In the case of PEO/mPPRNS-12%, where confinement dominates, the crystallization rate is substantially low. Although the confinement effects in the cases of PEO/PPRNSs are stronger owing to the higher orientations of PPRNSs, the crystallization rates are considerably higher than that of PEO/mPPRNS-12% due to the assistance of the nucleating effect. In the PEO/PPRNS system, both the confinement and nucleating effects coexist, aiding in controlling crystalline orientation.

To further support the nucleating effect of PPRNS, morphology evolution with respect to different PPRNS loadings was analyzed to investigate the crystallization mechanism (Supporting Information Figure S2). With an increase in the PPRNS loading to 6 wt %, the sizes of PEO crystals become smaller as compared to those in the cases of PEO and PEO/PPRNS-1%, suggesting the production of more nucleation sites in the same area. This demonstrates that PPRNSs act as nucleating agents, promoting the formation of additional nucleation sites and thus altering the crystallization behavior of PEO. Moreover, the potentials of grafted polymer brushes to direct the growths of polymer crystals are supported by simulation studies.<sup>42</sup> This characteristic is notable because of not only its ability to accelerate the crystallization rate, but also its impact on the structures of PEO crystals and preservation of these crystalline structures. This observation is significant considering that conventional methods relying on confinement effects often compromise the integrity of the crystalline structure. Retention of  $X_c$  holds importance in maintaining the physical and mechanical properties of semicrystalline polymers.

## DISCUSSION

Our investigation highlights the considerable capacities of PPRNSs to govern the orientations of crystallites in semicrystalline polymers. Even in a small amount of 1 wt %, PPRNSs induced anisotropic crystal orientations in PEO, with flat-on PEO lamellae aligning parallel to the film surfaces. Degree of PEO crystal orientation directly correlated with the concentrations of PPRNSs added, revealing the influential roles of PPRNSs in shaping crystalline structures. Additionally,

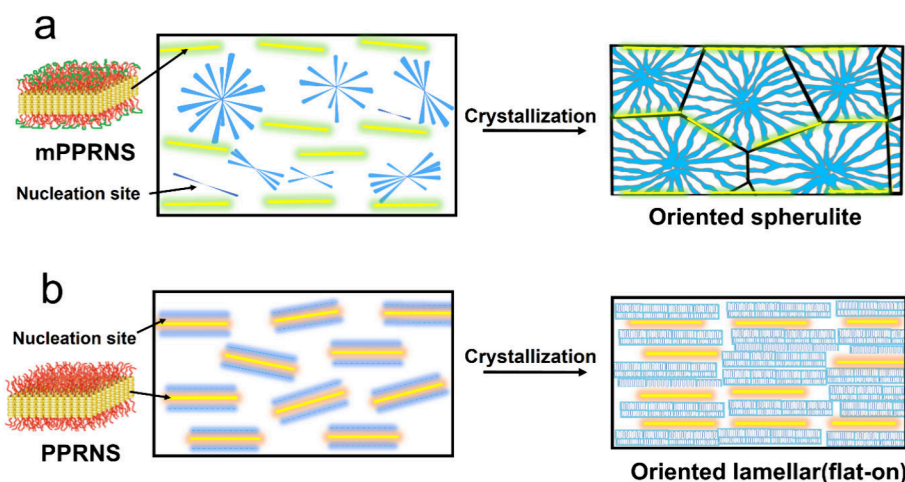


**Figure 5.** Schematics of crystallization: (a) Modified PPRNS-induced crystallization exclusively exhibiting the confinement effect along with a confined spherulite; (b) PPRNS-induced crystallization demonstrating polymer brush-initiated crystallization, featuring oriented and continuous PEO lamellar growth.

PPRNSs not only affected crystal morphologies including crystal growth direction, but also preserved  $X_c$ , which is a rare phenomenon in semicrystalline polymer nanocomposites comprising 2D fillers. Our control experiments, involving end-capping of the extended polymer brushes, further elucidated crystallization. As illustrated in Figure 5, two different crystallization mechanisms are observed and discussed as follows.

High abilities of PPRNSs to orient the crystal structure of the PEO matrix are attributed to several characteristics: (1) excellent dispersibility in the matrix, which is a major advantage; (2) the 2D nanosheet structure, which provides effective confinement and naturally aligns parallel to the film surface; and (3) presence of PEO brushes on the surface, which act as nucleation sites. These properties collectively enable PPRNSs to confine the crystal growth of the matrix in the in-plane direction, resulting in high orientation in the matrix crystal direction. In PEO/PPRNSs, both confinement and nucleation effects coexist and compete, leading to a balanced scenario where crystallization orientation and  $X_c$  are well-maintained.

In contrast, mPPRNSs exhibit lower abilities to serve as nucleation sites and orient the PEO matrix crystals owing to their bulky axis ends. Consequently, their behaviors are similar to those of traditional 2D fillers. In PEO nanocomposites containing mPPRNSs, nucleation primarily occurs in the matrix away from mPPRNSs. During crystallization, the PEO crystals are confined by mPPRNSs, causing them to push mPPRNSs aside, resulting in the accumulation of mPPRNSs at the boundary or their entrapment in the spherulite as shown in Figure 5a. This confinement disrupts the orientations of mPPRNSs during crystallization.

These insights demonstrate the unique advantages of PPRNSs over traditional 2D fillers, such as graphene and clay. The key distinction lies in PPRNSs' ability to combine physical confinement with interaction through their polymer brushes. While traditional 2D fillers like graphene or clay platelets rely solely on physical confinement, PPRNSs provide both spatial constraint and nucleation sites through their extended polymer brushes. This dual functionality enables precise control over crystal orientation while maintaining high

crystallinity, a combination rarely achieved with conventional fillers.

Furthermore, our study not only contributes to fundamental understanding, but also opens avenues for the design and development of innovative materials with tailored properties for diverse applications. Because of their unique characteristics, PPRNSs are promising candidates for the advancement of high-performance polymer nanocomposites, offering significant potential for transformative impact across various industries. Particularly, our findings pave the way for the development of biorelated materials with customized attributes and applications in numerous fields, for example, biomedicine, electronics, and environmental engineering.<sup>43</sup> For instance, in biomedicine, regulated orientations of crystallites can considerably impact the release kinetics of drugs confined in the polymer matrix, enabling precise control over therapeutic delivery mechanisms. Similarly, in electronic devices such as sensors and actuators, the incorporation of aligned crystalline structures can impart superior mechanical properties to these devices, leading to high performances and reliabilities of electronic systems.

## CONCLUSION

In conclusion, our study demonstrates the multifaceted potentials of PPRNSs in determining the properties and functionalities of polymer nanocomposites. Utilizing the exceptional properties of PPRNSs, we can create tailor-made materials with high performances and versatilities, addressing challenges and driving innovation across a wide range of industries. As research in this field is continuously advancing, we anticipate further breakthroughs that will reveal new opportunities for the application of PPRNS-based materials in various sectors, eventually contributing to the advancement of science and technology for the benefit of society.

## ASSOCIATED CONTENT

### Supporting Information

The Supporting Information is available free of charge at <https://pubs.acs.org/doi/10.1021/acs.macromol.4c02113>.

X-ray, SEM, and DSC results (PDF)



## AUTHOR INFORMATION

### Corresponding Authors

**Shuntaro Uenuma** – Department of Advanced Materials Science, Graduate School of Frontier Sciences, The University of Tokyo, Kashiwa, Chiba 277-8561, Japan; Research Center for Macromolecules and Biomaterials, National Institute for Materials Science (NIMS), Tsukuba, Ibaraki 305-0047, Japan; [orcid.org/0000-0003-0693-9310](https://orcid.org/0000-0003-0693-9310); Email: [s-uenuma@g.ecc.u-tokyo.ac.jp](mailto:s-uenuma@g.ecc.u-tokyo.ac.jp)

**Kohzo Ito** – Department of Advanced Materials Science, Graduate School of Frontier Sciences, The University of Tokyo, Kashiwa, Chiba 277-8561, Japan; Research Center for Macromolecules and Biomaterials, National Institute for Materials Science (NIMS), Tsukuba, Ibaraki 305-0047, Japan; [orcid.org/0000-0002-1798-3811](https://orcid.org/0000-0002-1798-3811); Email: [kohzo@k.u-tokyo.ac.jp](mailto:kohzo@k.u-tokyo.ac.jp)

### Authors

**Cong Liu** – Department of Advanced Materials Science, Graduate School of Frontier Sciences, The University of Tokyo, Kashiwa, Chiba 277-8561, Japan; Research Center for Macromolecules and Biomaterials, National Institute for Materials Science (NIMS), Tsukuba, Ibaraki 305-0047, Japan

**Sinan Feng** – Research Center for Negative Emissions Technologies, Kyushu University, Fukuoka 819-0395, Japan

**Shota Ando** – Department of Advanced Materials Science, Graduate School of Frontier Sciences, The University of Tokyo, Kashiwa, Chiba 277-8561, Japan

**Hideaki Yokoyama** – Department of Advanced Materials Science, Graduate School of Frontier Sciences, The University of Tokyo, Kashiwa, Chiba 277-8561, Japan; [orcid.org/0000-0002-0446-7412](https://orcid.org/0000-0002-0446-7412)

**Atsushi Takahara** – Research Center for Negative Emissions Technologies, Kyushu University, Fukuoka 819-0395, Japan; [orcid.org/0000-0002-0584-1525](https://orcid.org/0000-0002-0584-1525)

Complete contact information is available at:

<https://pubs.acs.org/10.1021/acs.macromol.4c02113>

### Author Contributions

K.I., S.U., and C.L. conceived the concept and designed the experiments. C.L. and S.F. conducted the experiments and analyzed the data. S.A. assisted with X-ray measurements. K.I. and S.U. supervised the overall project. C.L., S.F., S.U., H.Y., A.T., and K.I. cowrote the manuscript. All authors contributed to the discussion of the results and the manuscript. These authors contributed equally: C.L. and S.F.

### Notes

The authors declare no competing financial interest.

## ACKNOWLEDGMENTS

This work was supported by JST-Mirai Program Grant Number JPMJMI18A2, JSPS KAKENHI Grant Numbers JP19H00907 and JP21K14477, and NEDO Grant Number JPNP18016. Special thanks to Haruki Kazumi for assistance in obtaining AFM images and to Di Liu for help in the synthesis of modified PPRNSs.

## REFERENCES

- (1) Galeski, A. Strength and Toughness of Crystalline Polymer Systems. *Prog. Polym. Sci.* **2003**, *28* (12), 1643–1699.
- (2) Krigbaum, W. R.; Roe, R.-J.; Smith, K. J. A Theoretical Treatment of the Modulus of Semi-Crystalline Polymers. *Polymer* **1964**, *5*, 533–542.
- (3) Schmidt-Mende, L.; Fechtenkötter, A.; Müllen, K.; Moons, E.; Friend, R. H.; MacKenzie, J. D. Self-Organized Discotic Liquid Crystals for High-Efficiency Organic Photovoltaics. *Science* **2001**, *293* (5532), 1119–1122.
- (4) Wang, H.; Keum, J. K.; Hiltner, A.; Baer, E.; Freeman, B.; Rozanski, A.; Galeski, A. Confined Crystallization of Polyethylene Oxide in Nanolayer Assemblies. *Science* **2009**, *323* (5915), 757–760.
- (5) Shrestha, R.; Li, P.; Chatterjee, B.; Zheng, T.; Wu, X.; Liu, Z.; Luo, T.; Choi, S.; Hippalgaonkar, K.; de Boer, M. P.; Shen, S. Crystalline Polymer Nanofibers with Ultra-High Strength and Thermal Conductivity. *Nat. Commun.* **2018**, *9* (1), 1664.
- (6) Salleo, A. Charge Transport in Polymeric Transistors. *Mater. Today* **2007**, *10* (3), 38–45.
- (7) Wu, H.-C.; Nikzad, S.; Zhu, C.; Yan, H.; Li, Y.; Niu, W.; Matthews, J. R.; Xu, J.; Matsuhisa, N.; Arunachala, P. K.; Rastak, R.; Linder, C.; Zheng, Y.-Q.; Toney, M. F.; He, M.; Bao, Z. Highly Stretchable Polymer Semiconductor Thin Films with Multi-Modal Energy Dissipation and High Relative Stretchability. *Nat. Commun.* **2023**, *14* (1), 8382.
- (8) Wittmann, J. C.; Lotz, B. Epitaxial Crystallization of Polymers on Organic and Polymeric Substrates. *Prog. Polym. Sci.* **1990**, *15* (6), 909–948.
- (9) Schrauwen, B. A. G.; Breemen, L. C. A. v.; Spoelstra, A. B.; Govaert, L. E.; Peters, G. W. M.; Meijer, H. E. H. Structure, Deformation, and Failure of Flow-Oriented Semicrystalline Polymers. *Macromolecules* **2004**, *37* (23), 8618–8633.
- (10) Sawai, D.; Takahashi, K.; Sasashige, A.; Kanamoto, T.; Hyon, S.-H. Preparation of Oriented  $\beta$ -Form Poly(L-Lactic Acid) by Solid-State Coextrusion: Effect of Extrusion Variables. *Macromolecules* **2003**, *36* (10), 3601–3605.
- (11) Fukuya, M. N.; Senoo, K.; Kotera, M.; Yoshimoto, M.; Sakata, O. Controlling of Crystallite Orientation for Poly(Ethylene Oxide) Thin Films with Cellulose Single Nano-Fibers. *Polymer* **2014**, *55* (16), 4401–4404.
- (12) Shimada, E. S. E.; Uchida, T. U. T. Control of Polymer Orientation in Polymer Dispersed Liquid Crystal (PDLC). *Jpn. J. Appl. Phys.* **1992**, *31* (3B), L352.
- (13) Mohammadi, E.; Zhao, C.; Meng, Y.; Qu, G.; Zhang, F.; Zhao, X.; Mei, J.; Zuo, J.-M.; Shukla, D.; Diao, Y. Dynamic-Template-Directed Multiscale Assembly for Large-Area Coating of Highly-Aligned Conjugated Polymer Thin Films. *Nat. Commun.* **2017**, *8* (1), 16070.
- (14) Huang, H.-D.; Xu, J.-Z.; Fan, Y.; Xu, L.; Li, Z.-M. Poly(L-Lactic Acid) Crystallization in a Confined Space Containing Graphene Oxide Nanosheets. *J. Phys. Chem. B* **2013**, *117* (36), 10641–10651.
- (15) Zhao, M.; Wu, H.-M.; Zhu, Z.; Wu, J.-L.; Kang, W.-H.; Sue, H.-J. Preparation of Polyethylene Nanocomposites Based on Polyethylene Grafted Exfoliated  $\alpha$ -Zirconium Phosphate. *Macromolecules* **2022**, *55* (8), 3039–3050.
- (16) Wong, M.; Ishige, R.; White, K. L.; Li, P.; Kim, D.; Krishnamoorti, R.; Gunther, R.; Higuchi, T.; Jinnai, H.; Takahara, A.; Nishimura, R.; Sue, H.-J. Large-Scale Self-Assembled Zirconium Phosphate Smectic Layers via a Simple Spray-Coating Process. *Nat. Commun.* **2014**, *5* (1), 3589.
- (17) Maiz, J.; Martin, J.; Mijangos, C. Confinement Effects on the Crystallization of Poly(Ethylene Oxide) Nanotubes. *Langmuir* **2012**, *28* (33), 12296–12303.
- (18) Jiang, Q.; Ward, M. D. Crystallization under Nanoscale Confinement. *Chem. Soc. Rev.* **2014**, *43* (7), 2066–2079.
- (19) Uenuma, S.; Endo, K.; Yamada, N. L.; Yokoyama, H.; Ito, K. Polymer Brush Formation Assisted by the Hierarchical Self-Assembly of Topological Supramolecules. *ACS Appl. Mater. Interfaces* **2021**, *13* (50), 60446–60453.
- (20) Uenuma, S.; Maeda, R.; Yokoyama, H.; Ito, K. Autonomously Isolated Pseudo-Polyrotaxane Nanosheets Fabricated via Hierarchical

cally Ordered Supramolecular Self-Assembly. *Chem. Commun.* **2019**, 55 (29), 4158–4161.

(21) Uenuma, S.; Maeda, R.; Yokoyama, H.; Ito, K. Formation of Isolated Pseudo-Polyrotaxane Nanosheet Consisting of  $\alpha$ -Cyclodextrin and Poly(Ethylene Glycol). *Macromolecules* **2019**, 52 (10), 3881–3887.

(22) Jimenez, A. M.; Krauskopf, A. A.; Pérez-Camargo, R. A.; Zhao, D.; Pribyl, J.; Jestin, J.; Benicewicz, B. C.; Müller, A. J.; Kumar, S. K. Effects of Hairy Nanoparticles on Polymer Crystallization Kinetics. *Macromolecules* **2019**, 52 (23), 9186–9198.

(23) Kumar, S. K.; Jouault, N.; Benicewicz, B.; Neely, T. Nanocomposites with Polymer Grafted Nanoparticles. *Macromolecules* **2013**, 46 (9), 3199–3214.

(24) Zheng, Y.; Bruening, M. L.; Baker, G. L. Crystallization Kinetics of Polymer Brushes with Poly(Ethylene Oxide) Side Chains. *J. Polym. Sci., Part B: Polym. Phys.* **2010**, 48 (18), 1955–1959.

(25) Zheng, Y.; Bruening, M. L.; Baker, G. L. Crystallization of Polymer Brushes with Poly(Ethylene Oxide) Side Chains. *Macromolecules* **2007**, 40 (23), 8212–8219.

(26) Tsai, C.-C.; Leng, S.; Jeong, K.-U.; Van Horn, R. M.; Wang, C.-L.; Zhang, W.-B.; Graham, M. J.; Huang, J.; Ho, R.-M.; Chen, Y.; Lotz, B.; Cheng, S. Z. D. Supramolecular Structure of  $\beta$ -Cyclodextrin and Poly(Ethylene Oxide)-Block-Poly(Propylene Oxide)-Block-Poly(Ethylene Oxide) Inclusion Complexes. *Macromolecules* **2010**, 43 (22), 9454–9461.

(27) Uenuma, S.; Shikano, Y.; Liu, D.; Yokoyama, H.; Ito, K. Suppression of Supramolecular Disassembly of Pseudopolyrotaxane Nanosheet by End-Capping via Amine-Epoxy Click Reaction of Bifunctional Epoxy. *Macromolecules* **2023**, 56 (20), 8192–8198.

(28) Wunderlich, B. Chapter VIII - Equilibrium Melting. In *Macromolecular Physics*; Wunderlich, B., Ed.; Academic Press: San Diego, 1980; pp 1–127.

(29) Takahashi, Y.; Tadokoro, H. Structural Studies of Polyethers,  $-(\text{CH}_2\text{m}-\text{O})_n$ . X. Crystal Structure of Poly (Ethylene Oxide). *Macromolecules* **1973**, 6 (5), 672–675.

(30) Boles, M. A.; Engel, M.; Talapin, D. V. Self-Assembly of Colloidal Nanocrystals: From Intricate Structures to Functional Materials. *Chem. Rev.* **2016**, 116 (18), 11220–11289.

(31) Vargo, E.; Ma, L.; Li, H.; Zhang, Q.; Kwon, J.; Evans, K. M.; Tang, X.; Tovmasyan, V. L.; Jan, J.; Arias, A. C.; Destailats, H.; Kuzmenko, I.; Ilavsky, J.; Chen, W.-R.; Heller, W.; Ritchie, R. O.; Liu, Y.; Xu, T. Functional Composites by Programming Entropy-Driven Nanosheet Growth. *Nature* **2023**, 623 (7988), 724–731.

(32) Nam, J. Y.; Sinha Ray, S.; Okamoto, M. Crystallization Behavior and Morphology of Biodegradable Polylactide/Layered Silicate Nanocomposite. *Macromolecules* **2003**, 36 (19), 7126–7131.

(33) Sinha Ray, S.; Okamoto, M. Polymer/Layered Silicate Nanocomposites: A Review from Preparation to Processing. *Prog. Polym. Sci.* **2003**, 28 (11), 1539–1641.

(34) Alexandre, M.; Dubois, P. Polymer-Layered Silicate Nanocomposites: Preparation, Properties and Uses of a New Class of Materials. *Mater. Sci. Eng. R Rep.* **2000**, 28 (1), 1–63.

(35) Chu, C.-Y.; Chen, M.-H.; Wu, M.-L.; Chen, H.-L.; Chiu, Y.-T.; Chen, S.-M.; Huang, C.-H. Hierarchical Structure and Crystal Orientation in Poly(Ethylene Oxide)/Clay Nanocomposite Films. *Langmuir* **2014**, 30 (10), 2886–2895.

(36) Habel, C.; Maiz, J.; Olmedo-Martínez, J. L.; López, J. V.; Breu, J.; Müller, A. J. Competition between Nucleation and Confinement in the Crystallization of Poly(Ethylene Glycol)/ Large Aspect Ratio Hectorite Nanocomposites. *Polymer* **2020**, 202, 122734.

(37) Fernández, M. J.; Fernández, M. D. Effect of Organic Modifier and Clay Content on Non-Isothermal Cold Crystallization and Melting Behavior of Polylactide/Organovermiculite Nanocomposites. *Polymers* **2020**, 12 (2), 364.

(38) Badrinarayanan, P.; Ko, F. K.; Wang, C.; Richard, B. A.; Kessler, M. R. Investigation of the Effect of Clay Nanoparticles on the Thermal Behavior of PLA Using a Heat Flux Rapid Scanning Rate Calorimeter. *Polym. Test.* **2014**, 35, 1–9.

(39) Müller, A.; Arnal, M.; Trujillo, M.; Lorenzo, A. Super-Nucleation in Nanocomposites and Confinement Effects on the Crystallizable Components within Block Copolymers, Miktoarm Star Copolymers and Nanocomposites. *Eur. Polym. J.* **2011**, 47, 614–629.

(40) Meldrum, F. C.; O'Shaughnessy, C. Crystallization in Confinement. *Adv. Mater.* **2020**, 32 (31), 2001068.

(41) Liu, G.; Müller, A. J.; Wang, D. Confined Crystallization of Polymers within Nanopores. *Acc. Chem. Res.* **2021**, 54 (15), 3028–3038.

(42) Ming, Y.; Zhou, Z.; Hao, T.; Nie, Y.; Wei, Y.; Zhang, S.; Gao, W. Insights into the Crystallization of Polymer Nanocomposite Systems Blended with Grafted and Free Chains Studied by Molecular Simulation. *Cryst. Growth Des.* **2021**, 21 (4), 2243–2254.

(43) Wegst, U. G. K.; Bai, H.; Saiz, E.; Tomsia, A. P.; Ritchie, R. O. Bioinspired Structural Materials. *Nat. Mater.* **2015**, 14 (1), 23–36.